crystals

MDPI

Article

Enhanced Photoresponsivity of 2H-$MoTe_2$ by Inserting 1T-$MoTe_2$ Interlayer Contact for Photodetector Applications

Der-Yuh Lin [1,*], Hung-Pin Hsu [2,*], Guang-Hsin Liu [1], Ting-Zhong Dai [1] and Yu-Tai Shih [3]

[1] Department of Electronic Engineering, National Changhua University of Education, No. 2, Shi-Da Road, Changhua City 500, Taiwan; kevin860413@gmail.com (G.-H.L.); M0853009@cc.ncue.edu.tw (T.-Z.D.)
[2] Department of Electronic Engineering, Ming Chi University of Technology, No. 84, Gongzhuan Road, New Taipei City 24301, Taiwan
[3] Department of Physics, National Changhua University of Education, No. 2, Shi-Da Road, Changhua City 500, Taiwan; ytshih@cc.ncue.edu.tw
* Correspondence: dylin@cc.ncue.edu.tw (D.-Y.L.); hphsu@mail.mcut.edu.tw (H.-P.H.)

Abstract: The 2H molybdenum telluride ($MoTe_2$) photodetector structures were made with inserting 1T-$MoTe_2$ interlayer contacts. The optical response properties such as photoconductivity (PC) spectroscopy, illumination intensity dependent photoresponsivity, frequency dependent photocurrent, and time-resolved photoresponse were carried out in this study. In PC spectra, a much higher photoresponsivity of 2H-$MoTe_2$ were observed by inserting 1T-$MoTe_2$ interlayer contact. The frequency dependent photocurrent and time-resolved photoresponse investigations explore the carrier kinetic decay process of $MoTe_2$ with different electrode contact. The Schottky barrier heights (SBH) extracted by thermionic emission theory were also investigated by inserting 1T-$MoTe_2$ interlayer contacts. The results show the potential applicability for photodetection devices based $MoTe_2$ layered transition metal dichalcogenides semiconductors.

Keywords: $MoTe_2$; photoconductivity; photoresponse

Citation: Lin, D.-Y.; Hsu, H.-P.; Liu, G.-H.; Dai, T.-Z.; Shih, Y.-T. Enhanced Photoresponsivity of 2H-$MoTe_2$ by Inserting 1T-$MoTe_2$ Interlayer Contact for Photodetector Applications. *Crystals* **2021**, *11*, 964. https://doi.org/10.3390/cryst11080964

Academic Editor: Cyril Cayron

Received: 26 July 2021
Accepted: 15 August 2021
Published: 16 August 2021

Publisher's Note: MDPI stays neutral with regard to jurisdictional claims in published maps and institutional affiliations.

Copyright: © 2021 by the authors. Licensee MDPI, Basel, Switzerland. This article is an open access article distributed under the terms and conditions of the Creative Commons Attribution (CC BY) license (https://creativecommons.org/licenses/by/4.0/).

1. Introduction

The discovery of single layered graphene opened up new possibilities and research for the characteristics of two-dimensional (2D) materials [1,2]. The 2D transition metal dichalcogenides (TMDCs) are usually in MX_2 type where M stands for the transition metal from group IV-VII and X is the chalcogen elements S, Se, and Te [3–5]. Compare to graphene, TMDCs can be semiconductors, semi-metals, metals, or even superconductors. Such properties make them highly attractive for lots of studies of novel physical phenomena [6]. TMDCs layered 2D materials with atomic thickness are promising due to their potential use in nanoelectronics and optoelectronics for next generation devices [7,8], such as fin-shaped field effect transistors (FET) [9], FET with sub-10 nm channel length [10], inverter [11], on-chip light emitting diode [12], and Van der Walls heterostructure devices [13]. The most common used TMDCs such as MoS_2 and $MoSe_2$ have a band gap of 1.85 [14] and 1.55 [15] eV, respectively. The optical gap can be continuously tuned between the limits of the stoichiometric crystals using alloys with different chalcogen concentration. However, the design of band structure tailoring is an important issue for heterostructure devices. Hence, a material with a band gap close to 1 eV would be valuable in the building block for complex 2D structure system. Two hexagonal (2H) type molybdenum ditelluride ($MoTe_2$) is one of the typical 2D TMDCs, which has an indirect bandgap of about 0.9 eV [16] in bulk form and a direct bandgap of 1.1 eV by varying its thickness to monolayer [17]. To date, $MoTe_2$ has received much attention due to its rich crystalline phases and its unusual semiconducting, metallic and superconducting properties behaviors [18–20]. $MoTe_2$ also has been demonstrated as a promising material for the applications of nanoelectronic devices [21–23]. The preparation and device applications of home/hetero- junction $MoTe_2$ were also investigated [24–26].

The contact engineering for 2D materials is a key technology for the applications of electronic devices [27,28]. Electrical contacts with excellent performance are another critical issue for nanoelectronics and optoelectronics to achieve low power consumption, fast photoresponse and effective spin injection [29,30]. The 2D TMDCs are metallic with octahedral (1T) crystal structure and semiconductive with hexagonal (2H) crystal structure. Phase engineering is a promising method to form 1T/2H phase interface in TMDCs material systems [31,32]. Among the many known TMDCs, $MoTe_2$ has shown potential in achieving the 1T/2H hetero interface. Theoretical simulations of the interface geometries have also been studied [33]. The 1T-$MoTe_2$ is a Weyl semimetal with extreme high carrier mobility and 2H phase $MoTe_2$ is semiconductor with direct bandgap [34,35]. Hence, the further exploration of electrical contacts properties in $MoTe_2$ layered materials via phase transformation engineering for device fabrication is not only interesting but also important.

In this work, the photoresponse properties by inserting 1T-$MoTe_2$ interlayer contact of 2H-$MoTe_2$ are investigated. The PC spectra, frequency dependent photocurrent and time-resolved photoresponse investigations explore the carrier kinetic decay process. The Schottky barrier heights (SBH) were extracted by thermionic emission theory and were also investigated by inserting 1T $MoTe_2$ interlayer contacts [36]. The results of electrical and optical characterizations for photodetection devices are determined and possible mechanisms are discussed.

2. Materials and Methods

The $MoTe_2$ single crystals were grown from the composite elements (Mo:99.99% and Te:99.99%) by the chemical-vapor transport method. The chemical transport was achieved with ICl_3 as transport agent. Total charge used in growth experiment was about 5 g. Prior to the crystal growth the powdered compounds of the series were prepared from the elements by reaction at 1000 °C for 10 days in evacuated quartz ampoules. The growth temperature was about 900 °C at the high temperature end and 800 °C for the low temperature end with a temperature gradient of about 3 °C/cm, and the growth time was about 20 days. Single layered crystals were formed in silver-colored platelets with a thickness of ~20 um and lateral size of 2 mm × 3 mm. For the preparation of 1T phase $MoTe_2$ interlayer as electrode contact material, the phase transformation from 2H to 1T phase is achieved by annealing process (at 700 °C, 120 min). After the phase transformation process, the 1T-$MoTe_2$ interlayer is connected on 2H-$MoTe_2$.

In PC measurements, the spectra were measured in the range from 0.7 to 1.55 eV by the probe beam with several mW with chopping frequency at ~10 Hz. A data acquisition (DAQ) device with time resolution of 1 ms was used for the time-resolved photoresponse measurement. For frequency-dependent photocurrent measurement, a 2 mW 980 nm laser was used as the excitation illumination. The steady state photocurrent at 0 Hz represented the dc photocurrent. The AC part represents the photocurrent induced in the frequency range of 0.5 to 10 kHz.

3. Results and Discussion

The phase properties of 2H-and 1T-$MoTe_2$ were first characterized by Raman spectra. In Figure 1a, the Raman peaks which are E_{2g} mode for 2H-$MoTe_2$ and B_g mode for 1T-$MoTe_2$, respectively [24]. In order to study the photoresponse properties of 2H-$MoTe_2$ with different electrode contact, we fabricate the $MoTe_2$ photodetector structure by inserting 1T-$MoTe_2$ as interlayer contact. For comparison purposes, a contact using Ag contact on 2H-$MoTe_2$ was also prepared. The schematic diagram of Ag and 1T-$MoTe_2$ interlayer electrode contacts of 2H-$MoTe_2$ structures are shown in Figure 1b.

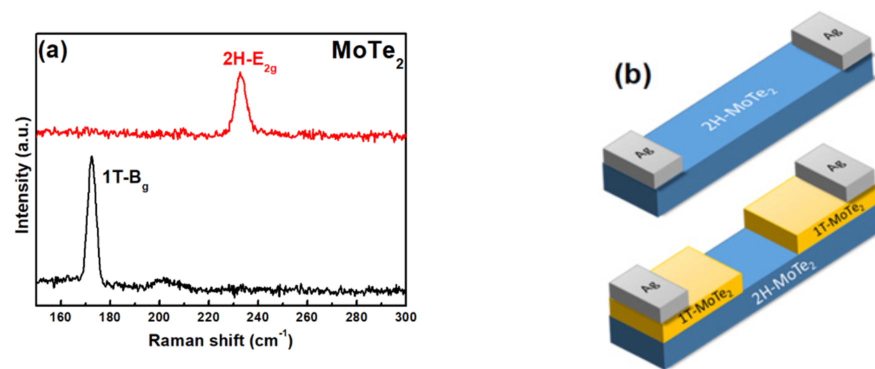

Figure 1. (**a**) Raman spectra of 2H- and 1T-$MoTe_2$. (**b**) The schematic diagram of Ag and 1T-$MoTe_2$ interlayer electrode contacts of 2H-$MoTe_2$ structures.

Figure 2 shows the photocurrent (PC) spectra of 2H-$MoTe_2$ with Ag and 1T-$MoTe_2$ interlayer electrode contacts. We can observe the peak arise from ~0.9 eV which was attributed to the energy gap of 2H-$MoTe_2$. It is also noticed here that the photoresponse of 2H-$MoTe_2$ was enhanced a lot by inserting 1T-$MoTe_2$ interlayer electrode contact.

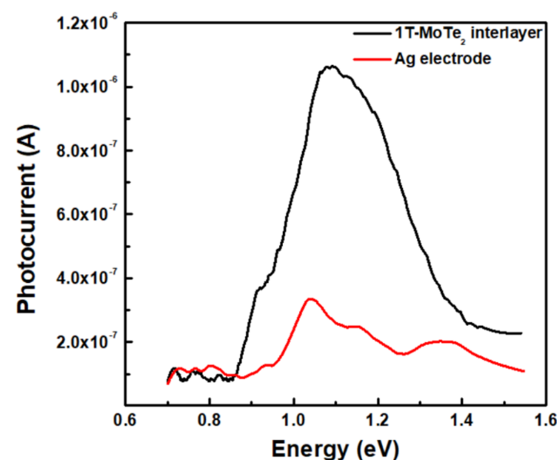

Figure 2. The PC spectra of Ag and 1T-$MoTe_2$ interlayer electrode contacts of 2H-$MoTe_2$ structures at 300 K.

Figure 3 shows the illumination intensity dependent photoresponsivity of using Ag and 1T-$MoTe_2$ interlayer electrode contacts of 2H-$MoTe_2$. The responsivity (R) is defined as the photocurrent generated per unit power of the incident illumination. It shows the responsivity decrease gradually with the increase of illumination intensity. The responsivity can be extracted from the experimental results by using the power law function $R = P^{-n}$ [37,38]. The power equation fits to the experimental data with an exponent (n); the exponent implies the mechanism of carrier recombination and trapping states during the photoresponse process. The obtained n is 0.57 for 1T-$MoTe_2$ interlayer electrode contacts of $MoTe_2$ which is correlated with the mechanism including recombination states and carrier–carrier interactions. However, we observe two slopes with Ag contact sample which means two different recombination mechanisms are involved.

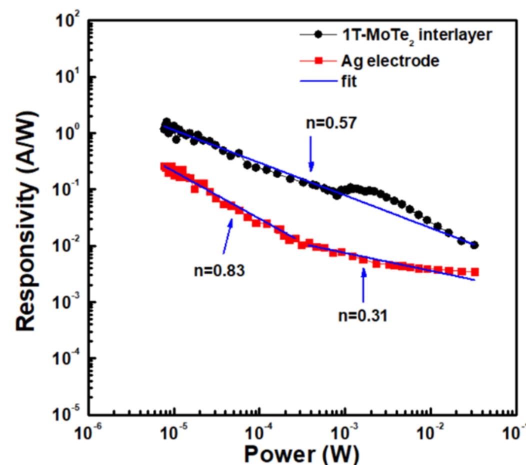

Figure 3. The photoresponsivity plotted with respect to illumination intensity for 2H-$MoTe_2$ using Ag and 1T-$MoTe_2$ interlayer electrode contacts.

The time-resolved photoresponse dynamics of Ag and 1T-$MoTe_2$ interlayer electrode contacts of 2H-$MoTe_2$ were measured by applying ON/OFF light modulation. Figure 4a,b shows the time-resolved photoresponse of Ag and 1T-$MoTe_2$ interlayer electrode contacts of 2H-$MoTe_2$ with the incident light frequencies of 1000 Hz. In time domain, the speed of photoresponse is characterized by the rise time (t_r) and the fall time (t_f). The rise time and fall time are defined as the time interval for the response rise from 10% to 90%, and decay from 90% to 10% of its maximum photocurrent value, respectively [39]. A single response cycle at 1000 Hz is shown in Figure 4c,d. The rise and fall times for Ag contact on 2H-$MoTe_2$ are 180 and 185 μs, respectively. Using 1T-$MoTe_2$ interlayer electrode contact reveals a faster rise time of 98 μs, as well as a shorter fall time of 99 μs, which indicate the photoresponse speed can be improved by using 1T-$MoTe_2$ as interlayer contact. The slower photoresponse in Ag contact on 2H-$MoTe_2$ might be due to the influence of trap state which deteriorates the carriers' transfer efficiency.

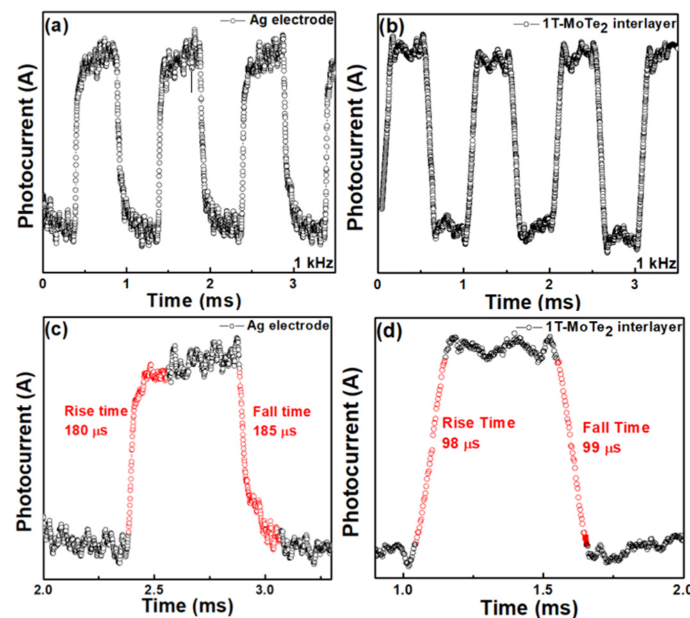

Figure 4. Time-resolved photoresponse of (**a**) Ag and (**b**) 1T-$MoTe_2$ interlayer electrode contacts of 2H-$MoTe_2$ structures at 1 kHz. The enlarged plots of (**c**) Ag and (**d**) 1T-$MoTe_2$ interlayer electrode contacts of 2H-$MoTe_2$ structures of one response cycle for calculating the rise and fall times.

In the applications of optoelectronic device, the photoconductivity was also investigated for the 2H-$MoTe_2$ using Ag and 1T-$MoTe_2$ interlayer electrode contacts. In order to understand the kinetics of the photoconductivity, the frequency dependence of the photoconductivity I_{ac}/I_{dc} was studied, where I_{ac} is the ac component of the photocurrent, and I_{dc} represents the steady state photocurrent. A laser diode with 980 nm wavelength is used as the illumination source. Figure 5 illustrates the frequency dependent photoconductivity of of Ag and 1T-$MoTe_2$ interlayer electrode contacts of 2H-$MoTe_2$. It is observed that I_{ac}/I_{dc} of Ag contact on 2H-$MoTe_2$ decreases faster than that of 1T-$MoTe_2$ interlayer electrode contact as frequency increase. The behaviour of frequency dependence PC can be described by the relation [40]:

$$I_{ac}/I_{dc} = k_1 \times \tanh\left(\frac{1}{4f\tau_1}\right) + k_2 \times \tanh\left(\frac{1}{4f\tau_2}\right) \quad (1)$$

where k_1 and k_2 are the amplitude coefficients. t_1 and t_2 are the carrier time constants of two decay processes. The obtained coefficients were listed in Table 1. These results indicate that the ratio of long-time constant decay process in Ag contact on $MoTe_2$ is larger than short time constant decay process, whereas in using 1T-$MoTe_2$ interlayer electrode contact, the 52% time constant is composed of short time constant decay process. This might attribute to the additional trap state in Ag contact on 2H-$MoTe_2$, which causes a longer time constant decay process.

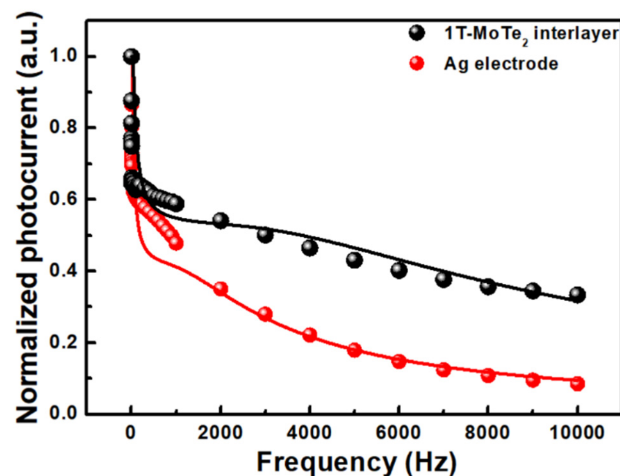

Figure 5. Normalized photoconductivity as a function of the frequency of Ag and 1T-$MoTe_2$ interlayer electrode contacts of 2H-$MoTe_2$.

Table 1. The obtained values of coefficients from the least-square fits to Equation (1) for the 2H-$MoTe_2$ using Ag and 1T-$MoTe_2$ interlayer electrode contacts.

Contact Type	Ag Electrode	1T-$MoTe_2$ Interlayer
k_1	0.61	0.48
k_2	0.39	0.52
τ_1	7.5 ms	3.8 ms
τ_2	105 us	35 us

The electrical resistivity as a function of temperature in the range from 20 to 300 K for both Ag and 1T-$MoTe_2$ interlayer electrode contacts of 2H-$MoTe_2$ are plotted in Figure 6. The results show the resistivity for both Ag and 1T-$MoTe_2$ interlayer electrode contacts of 2H-$MoTe_2$ decrease with increasing temperature. It is noticed here that the resistivity can be reduced by using 1T-$MoTe_2$ interlayer as electrode contact. This might be attributed to the better junction characteristic between the 1T metal and 2H semiconductor $MoTe_2$. We

further investigate the I-V characteristics of 2H-$MoTe_2$ with Ag and 1T-MoT_2 electrodes contact.

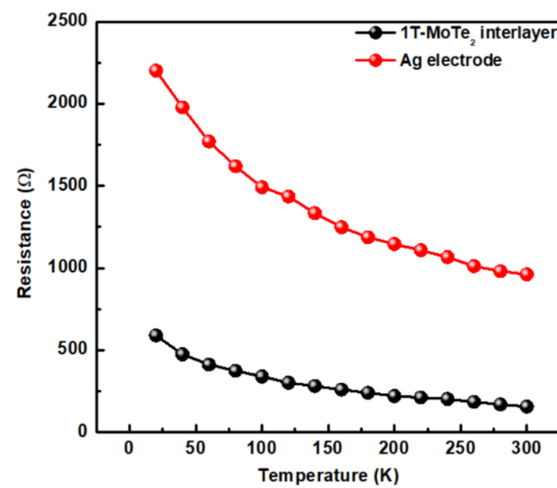

Figure 6. The resistance as a function of temperature in the range from 20 to 300 K for Ag and 1T-$MoTe_2$ interlayer electrode contacts of 2H-$MoTe_2$.

The forward I-V characteristics of an ideal Schottky junction can be expressed as [41]

$$I_f = I_s \exp\left(\frac{qVL_f}{k_B T}\right) \tag{2}$$

where

$$I_s = AST^2 \exp(-\frac{q\Phi_B}{k_B T}) \tag{3}$$

I_s is the diode saturation current, A is the Richardson constant, S is the contact area of junction, q is the electron charge, Φ_B is the Schottky barrier height, and k_B is the Boltzmann constant. As the carrier transport behavior in device is treated as the 2D material, the current I_{2D} can be defined by 2D thermionic emission model [42], which employs the reduced power law $T^{3/2}$ for a 2D transport channel:

$$I_{2D} = A^*_{2D} ST^{2/3} \exp[-\frac{q}{k_B T}(\Phi_B - \frac{V}{n})] \tag{4}$$

where ${A^*}_{2D}$ is the 2D equivalent Richardson constant, n is the ideality factor, and V is the voltage. To determine the Schottky barrier height, temperature dependent I-V measurements of 2H-$MoTe_2$ with Ag and 1T-$MoTe_2$ interlayer electrode contacts were carried out. To investigate the barrier, it is common to use Arrhenius plot. The $\ln(I_{2D}/T^{2/3})$ against 1000/T for various V in Figure 7a,c. By fitting the data to each V, we obtained the slope with Φ. Then by plotting the slope as a function of V. The Schottky barrier height can be extracted from the y intercept in Figure 7b,d. The Schottky barrier heights of Ag and 1T electrodes are 108.3 and 60.6 meV, respectively, which are shown in Table 2. The results demonstrate that the Schottky barrier height can be reduced by using 1T-$MoTe_2$ interlayer as electrode contact. The 2H-$MoTe_2$ by inserting 1T-$MoTe_2$ interlayer contact show an improvement in device performance compared to the one with Ag/2H contact, which might be due to the reduced contact resistance and smaller barrier height at interface [26]. Moreover, the reduced interface traps also lead to improve the carrier transport process across the interface which further produce better photoresponsivity properties.

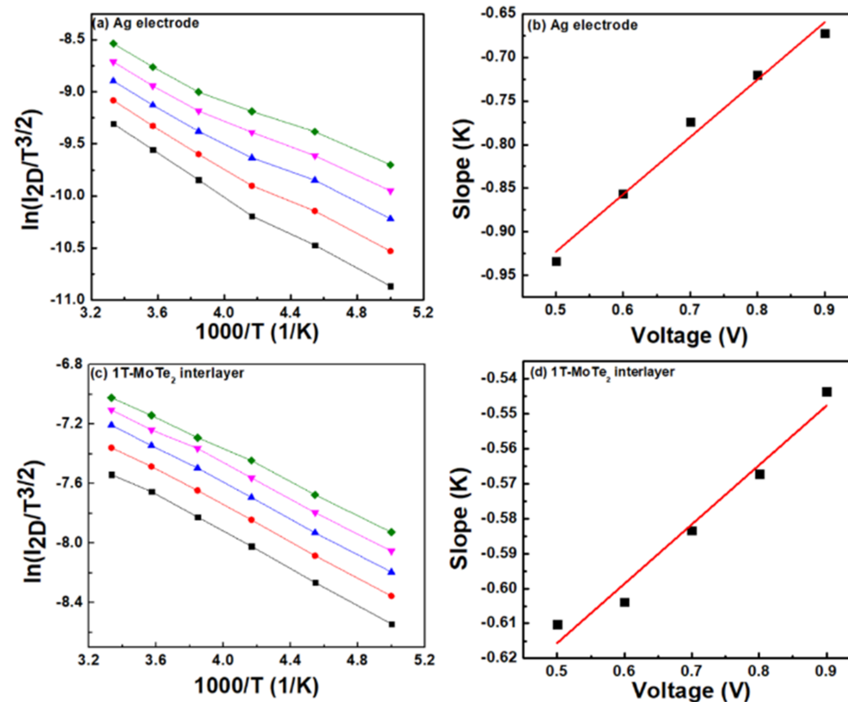

Figure 7. The Arrhenius plot. The $\ln(I_{2D}/T^{2/3})$ against 1000/T for various V for (**a**) Ag and (**c**) 1T-$MoTe_2$ interlayer electrode contacts of 2H-$MoTe_2$. Extracted of via Φ_B the y intercept value of (**b**) Ag and (**d**) 1T-$MoTe_2$ interlayer electrode contacts of 2H-$MoTe_2$.

Table 2. The Schottky barrier heights of Ag and 1T-$MoTe_2$ interlayer electrode contacts determined from 2D thermionic emission model.

Contact Type	Work Function (Φ_M)	Schottky Barrier Height (Φ_B)
Ag	4.26 eV	108.3 meV
1T-$MoTe_2$	4.10 eV	60.6 meV

4. Conclusions

In this report we have demonstrated that the photoresponse properties of 2H-$MoTe_2$ can be improved by inserting 1T-$MoTe_2$ interlayer contact. From PC spectra, we found that the light sensitive range did not change but the responsivity has been enhanced about 10 times. Furthermore, the illumination intensity dependent photoresponsivity study also confirmed that the responsivity has been enhanced more than one order in the whole intensity range from 1×10^{-5} to 3×10^{-2} W. About the response speed, the time-resolved photoresponse analysis shows that the rise time and fall time decrease from 180 to 98 µs and from 185 to 99 µs, respectively, after inserting 1T-$MoTe_2$ interlayer as contact. The frequency dependence photoconductivity investigation also revealed that short time constant response increases. The ratio was increased from about 40% for Ag electrode (k_2 = 0.39, in Table 1) to over 50% (k_2 = 0.52, in Table 1) after inserting 1T-$MoTe_2$ interlayer. We also demonstrated that the Schottky barrier heights can be reduced from about 108 to 60 meV. Our result showed that the interesting 1T-$MoTe_2$ interlayer as electrode contact is an easy and effective method to improve the photoresponse properties.

Author Contributions: H.-P.H. and D.-Y.L. conceived and designed the experiments. G.-H.L. and T.-Z.D. prepared the materials and performed the experiments. H.-P.H., D.-Y.L., and Y.-T.S. analyzed data. H.-P.H. and D.-Y.L. wrote the manuscript. All authors have read and agreed to the published version of the manuscript.

Funding: This work is supported by the Ministry of Science and Technology of Taiwan under project no. MOST. 109-2221-E-018-008.

Data Availability Statement: Not applicable.

Conflicts of Interest: The authors declare that they have no conflict of interest.

References

1. Nair, R.R.; Blake, P.; Grigorenko, A.N.; Novoselov, K.S.; Booth, T.J.; Statuber, T.; Prers, N.M.R.; Geim, A.K. Fine structure constant defines visual transparency of graphene. *Science* **2008**, *320*, 1308. [CrossRef]
2. Echtermeyer, T.J.; Britnell, L.; Jasnos, P.K.; Lombardo, A.; Gorbachev, R.V.; Grigorenko, A.N.; Geim, A.K.; Ferrari, A.C.; Novoselov, K.S. Strong plasmonic enhancement of photovoltage in graphene. *Nat. Commun.* **2011**, *2*, 458. [CrossRef] [PubMed]
3. Yoffe, A.D. Electronic Properties of Two Dimensional Solids: The Layer Type Transition Metal Dichalcogenides. *Festkörper Probl.* **1973**, *13*, 1–29.
4. Yoffe, A.D. Electronic properties of low dimensional solids: The physics and chemistry of layer type transition metal dichalcogenides and their intercalate complexes. *Solid State Ion.* **1990**, *39*, 1–7. [CrossRef]
5. Wilson, J.A.; Yoffe, A.D. The transition metal dichalcogenides discussion and interpretation of the observed optical, electrical and structural properties. *Adv. Phys.* **1969**, *18*, 193–335. [CrossRef]
6. Ganatra, R.; Zhang, Q. Few-layer MoS_2: A promising layered semiconductor. *ACS Nano* **2014**, *8*, 4074–4099. [CrossRef] [PubMed]
7. Wang, Q.; Kalantar-Zadeh, K.; Kis, A.; Coleman, J.N.; Strano, M.S. Electronics and optoelectronics of two-dimensional transition metal dichalcogenides. *Nat. Nanotech.* **2012**, *7*, 699–712. [CrossRef]
8. Radisavljevic, B.; Radenovic, A.; Brivio, J.; Giacometti, V.; Kis, A. Single-layer MoS_2 transistors. *Nat. Nanotech* **2011**, *6*, 147–150. [CrossRef]
9. Lan, Y.W.; Chen, P.C.; Lin, Y.Y.; Li, M.Y.; Li, L.J.; Tu, Y.L.; Yang, F.L.; Chen, M.C.; Li, K.S. Scalable fabrication of a complementary logic inverter based on MoS_2 fin-shaped field effect transistors. *Nanoscale Horiz.* **2019**, *4*, 683–688. [CrossRef]
10. Nourbakhsh, A.; Zubair, A.; Sajjad, R.N.; Amir Tavakkoli, K.G.; Chen, W.; Fang, S.; Ling, X.; Kong, J.; Dresselhaus, M.S.; Kaxiras, E.; et al. MoS_2 field-effect transistor with sub-10 nm channel length. *Nano Lett.* **2016**, *16*, 7798–7806. [CrossRef]
11. Tosun, M.; Chuang, S.; Fang, H.; Sachid, A.B.; Hettick, M.; Lin, Y.; Zeng, Y.; Javey, A. High-gain inverters based on WSe_2 complementary field-effect transistors. *ACS Nano* **2014**, *8*, 4948–4953. [CrossRef]
12. Withers, F.; Del Pozo-Zamudio, O.; Mishchenko, A.; Rooney, A.P.; Gholinia, A.; Watanabe, K.; Taniguchi, T.; Haigh, S.J.; Geim, A.K.; Tartakovskii, A.I.; et al. Light-emitting diodes by band-structure engineering in van der Waals heterostructures. *Nat. Mater.* **2015**, *14*, 301–306. [CrossRef] [PubMed]
13. Li, M.Y.; Shi, Y.; Cheng, C.C.; Lu, L.S.; Lin, Y.C.; Tang, H.L. Epitaxial growth of a monolayer WSe_2-MoS_2 lateral p-n junction with an atomically sharp interface. *Science* **2015**, *349*, 524–528. [CrossRef] [PubMed]
14. Mak, K.F.; Lee, C.; Hone, J.; Shen, J.; Heinz, T.F. Atomically thin MoS_2: A new direct-gap semiconductor. *Phys. Rev. Lett.* **2010**, *105*, 136805. [CrossRef] [PubMed]
15. Zhang, Y.; Chang, T.R.; Zhou, B.; Cui, Y.T.; Yan, H.; Liu, Z.; Schmitt, F.; Lee, J.; Moore, R.; Chen, Y.; et al. Direct observation of the transition from indirect to direct bandgap in atomically thin epitaxial $MoSe_2$. *Nat. Nanotech.* **2014**, *9*, 111–115. [CrossRef]
16. Yun, W.S.; Han, S.W.; Hong, S.C.; Kim, I.G.; Lee, J.D. Thickness and strain effects on electronic structures of transition metal dichalcogenides: 2H-MX_2 semiconductors (M = Mo, W; X = S, Se, Te). *Phys. Rev. B* **2012**, *85*, 033305. [CrossRef]
17. Ruppert, C.; Aslan, O.B.; Heinz, T.F. Optical properties and band gap of single- and few-layer $MoTe_2$. *Nano Lett.* **2014**, *14*, 6231–6236. [CrossRef]
18. Empante, T.A.; Zhou, Y.; Klee, V.; Nguyen, A.E.; Lu, I.H.; Valentin, M.D.; Naghibi Alvillar, A.A.; Preciado, E.; Berges, A.J.; Merida, C.S.; et al. Chemical Vapor Deposition Growth of Few-Layer $MoTe_2$ in the 2H, 1T′, and 1T Phases: Tunable Properties of $MoTe_2$ Films. *ACS Nano* **2017**, *11*, 900–905. [CrossRef]
19. Qi, Y.; Naumov, P.; Ali, M.N.; Rajamathi, C.R.; Schnelle, W.; Barkalov, O.; Hanfland, M.; Wu, S.C.; Shekhar, C.; Sun, Y.; et al. Superconductivity in Weyl semimetal candidate $MoTe_2$. *Nat. Commun.* **2016**, *7*, 11038. [CrossRef]
20. Deng, K.; Wan, G.; Deng, P.; Zhang, K.; Ding, S.; Wang, E.; Yan, M.; Huang, H.; Zhang, H.; Xu, Z.; et al. Experimental observation of topological Fermi arcs in type-II Weyl semimetal $MoTe_2$. *Nat. Phys.* **2016**, *12*, 1105–1110. [CrossRef]
21. Liu, X.; Islam, A.; Guo, J.; Feng, P.X.L. Controlling polarity of $MoTe_2$ transistors for monolithic complementary logic via Schottky contact engineering. *ACS Nano* **2020**, *14*, 1457–1467. [CrossRef]
22. Chang, Y.M.; Yang, S.H.; Lin, C.Y.; Chen, C.H.; Lien, C.H.; Jian, W.B.; Ueno, K.; Suen, Y.W.; Tsukagoshi, K.; Lin, Y.F. Reversible and precisely controllable p/n-type doping of $MoTe_2$ transistors through electrothermal doping. *Adv. Mater.* **2018**, *30*, 1706995. [CrossRef]
23. Lin, Y.F.; Xu, Y.; Wang, S.T.; Li, S.L.; Yamamoto, M.; Aparecido-Ferreira, A.; Li, W.; Sun, H.; Nakaharai, S.; Jian, W.B.; et al. Ambipolar $MoTe_2$ transistors and their applications in logic circuits. *Adv. Mater.* **2014**, *26*, 3263–3269. [CrossRef]
24. Yoo, Y.; DeGregorio, Z.P.; Su, Y.; Koester, S.J.; Johns, E. In-plane 2H-1T′ $MoTe_2$ homojunctions synthesized by flux-controlled phase engineering. *Adv. Mater.* **2017**, *29*, 1605461. [CrossRef]
25. Kim, H.; Johns, J.E.; Yoo, Y. Mixed-dimensional in-plane heterostructures from 1D Mo_6Te_6 and 2D $MoTe_2$ synthesized by Te-flux-controlled chemical vapor deposition. *Small* **2020**, *16*, 2002849. [CrossRef]
26. Ma, R.; Zhang, H.; Yoo, Y.; Degregorio, Z.P.; Jin, L.; Golani, P.; Azadani, J.G.; Low, T.; Johns, J.E.; Bendersky, L.A.; et al. $MoTe_2$ lateral homojunction field-effect transistors fabricated using flux-controlled phase engineering. *ACS Nano* **2019**, *13*, 8035–8046. [CrossRef]

27. Zhang, P.; Zhang, Y.; Wei, Y.; Jiang, H.; Wang, X.; Gong, Y. Contact engineering for two-dimensional semiconductors. *J. Semicond.* **2020**, *41*, 071901. [CrossRef]
28. Zheng, Y.; Gao, J.; Han, C.; Chen, W. Ohmic Contact Engineering for Two-Dimensional Materials. *Cell Rep. Phys. Sci.* **2021**, *2*, 100298. [CrossRef]
29. Léonard, F.; Talin, A.A. Electrical contacts to one- and two-dimensional nanomaterials. *Nat. Nanotech.* **2011**, *6*, 773–783. [CrossRef] [PubMed]
30. Allain, A.; Kang, J.; Banerjee, K.; Kis, A. Electrical contacts to two-dimensional semiconductors. *Nat. Mater.* **2015**, *14*, 1195–1205. [CrossRef] [PubMed]
31. Sung, J.H.; Heo, H.; Si, S.; Kim, Y.H.; Noh, H.R.; Song, K.; Kim, J.; Lee, C.S.; Seo, S.Y.; Kim, D.H.; et al. Coplanar semiconductor–metal circuitry defined on few-layer $MoTe_2$ via polymorphic heteroepitaxy. *Nat. Nanotech.* **2017**, *12*, 1064–1070. [CrossRef]
32. Lin, Y.C.; Dumcenco, D.O.; Huang, Y.S.; Suenage, K. Atomic mechanism of the semiconducting-to-metallic phase transition in single-layered MoS_2. *Nat. Nanotech.* **2014**, *9*, 391–396. [CrossRef]
33. Li, A.; Pan, J.; Dai, X.; Ouyang, F. Electrical contacts of coplanar 2H/1T′ $MoTe_2$ monolayer. *J. Appl. Phys.* **2019**, *125*, 075104. [CrossRef]
34. Keum, D.H.; Cho, S.; Kim, J.H.; Choe, D.H.; Sung, H.J.; Kan, M.; Kang, H.; Hwang, J.Y.; Kim, S.W.; Yang, H.; et al. Bandgap opening in few-layered monoclinic $MoTe_2$. *Nat. Phys.* **2015**, *11*, 482–486. [CrossRef]
35. Sankar, R.; Rao, G.N.; Muthuselvam, I.P.; Butler, C.; Kumar, N.; Senthil Murugan, G.; Shekhar, C.; Chang, T.R.; Wen, C.Y.; Chen, C.W.; et al. Polymorphic layered $MoTe_2$ from semiconductor, topological insulator, to Weyl semimetal. *Chem. Mater.* **2017**, *29*, 699–707. [CrossRef]
36. Wang, W.; Liu, Y.; Tang, L.; Jin, Y.; Zhao, T.; Xiu, F. Controllable Schottky Barriers between MoS_2 and Permalloy. *Sci. Rep.* **2014**, *4*, 6928. [CrossRef] [PubMed]
37. Lin, D.Y.; Jheng, J.J.; Ko, T.S.; Hsu, H.P.; Lin, C.F. Doping with Nb enhances the photoresponsivity of WSe_2 thin sheets. *AIP Adv.* **2018**, *8*, 055011. [CrossRef]
38. Zhang, X.; Liu, B.; Yang, W.; Jia, W.; Li, J.; Jiang, C.; Jiang, X. 3D-branched hierarchical 3C-SiC/ZnO heterostructures for high-performance photodetectors. *Nanoscale* **2016**, *8*, 17573–17580. [CrossRef] [PubMed]
39. Wu, D.; Jiang, Y.; Li, S.; Li, F.; Lan, X.; Zhang, Y.; Wu, C.; Luo, L.; Jie, J. Construction of high-quality CdS:Ga nanoribbon/silicon heterojunctions and their nano-optoelectronic applications. *Nanotechnology* **2011**, *22*, 405201. [CrossRef]
40. Ko, T.S.; Huang, C.C.; Lin, D.Y.; Ruan, Y.J.; Huang, Y.S. Electrical and optical properties of Co-doped and undoped MoS_2. *Jpn. J. Appl. Phys.* **2016**, *55*, 04EP06. [CrossRef]
41. Bhuiyan, A.S.; Martinez, A.; Esteve, D. A new Richardson plot for non-ideal schottky diodes. *Thin Solid Films* **1988**, *161*, 93–100. [CrossRef]
42. Anwar, A.; Nabet, B.; Culp, J.; Castro, F. Effects of electron confinement on thermionic emission current in a modulation doped heterostructure. *J. Appl. Phys.* **1999**, *85*, 2663–2666. [CrossRef]